Check for updates

LASER & PHOTONICS REVIEWS
www.lpr-journal.org

All-Dielectric High-Q Dynamically Tunable Transmissive Metasurfaces

*Ruzan Sokhoyan, Claudio U. Hail, Morgan Foley, Meir Y. Grajower, and Harry A. Atwater**

Active metasurfaces, which are arrays of actively tunable resonant elements, can dynamically control the wavefront of the scattered light at a subwavelength scale. To date, most active metasurfaces that enable dynamic wavefront shaping operate in reflection. On the other hand, active metasurfaces operating in transmission are of considerable interest as they can readily be integrated with chip-scale light sources, yielding ultra-compact wavefront shaping devices. Here, designs for all-dielectric low-loss active metasurfaces which can dynamically manipulate the transmitted light wavefront in the near-infrared wavelength range are reported. The active metasurfaces feature an array of amorphous silicon (a-Si) pillars on a silica (SiO_2) substate, which support resonances with quality factors (Q-factors) as high as 9800. The high-Q resonance dips observed in transmission can be transformed into transmission resonance peaks by positioning a-Si pillar resonators at a prescribed distance from a crystalline Si substrate. The design of metasurface geometry with realistic interconnect architectures that enable thermo-optic dynamic beam switching with switching times as low as 7.3 µs is reported. Beam switching is observed for refractive index differences between neighboring metasurface elements as low as 0.0026. It is shown that the metasurface structures with realistic interconnect architectures can be used for dynamic beam steering.

1. Introduction

The prospect of creating chip-scale ultracompact optical components that can be dynamically programmed to scatter or emit light with an arbitrarily shaped wavefront has long captivated researchers. Realization of chip-scale dynamically programmable optical components operating in the near-infrared or visible wavelength range could be instrumental for important applications, such as light detection and ranging (LiDAR), free space optical communications, additive manufacturing, and directed energy. The quest for these chip-scale spatial light modulators has motivated intensive research efforts in the design of active metasurfaces.[1–3] A prototypical active metasurface is composed of an array of geometrically identical subwavelength resonant metasurface elements which can dynamically control the phase and amplitude of light scattered by each metasurface element.[4] Recent reports[1,5] have experimentally demonstrated programmable metasurface chips with electric field effect control of the phase of light scattered by each metasurface element. Dynamic control of the phase at a subwavelength scale has enabled the experimental realization of beam steering and reconfigurable focusing using the same metasurface structure.[1] Notably, this demonstration[1] and the majority of other experimentally reported active metasurfaces operate in reflection. Operation in reflection mode dictates that the illuminating light source is located off-chip, which would unavoidably increase the form factor of the resulting optical system. Moreover, a reflection configuration for the illuminating light source may limit versatility since part of the metasurface aperture will be blocked by the light source. Transmissive metasurfaces, on the other hand, have the potential to yield more compact monolithic optical systems, since they allow for integration with chip-based light sources such as vertical cavity surface emitting lasers (VCSELs)[6] or photonic cavity surface emitting lasers (PCSELs).[7]

Dynamic amplitude-tunable transmissive metasurfaces have been experimentally demonstrated using indium tin oxide (ITO) field effect modulation,[8,9] conductive polymer electrochemical transitions,[10] ionic transport,[11] Pockels effect in organic molecules,[12] and thermo-optic effect in silicon (Si).[13] Several researchers[9,10] have utilized transmittance modulation to achieve diffractive beam switching with modest efficiencies. However, dynamically tunable phase control is also a prerequisite for versatile wavefront manipulation. Recent experiments have demonstrated dynamic beam switching in transmission using reorientation of liquid crystals in which a degree of phase control has contributed to the observed dynamic beam switching.[2] Previous works have also used dielectric elastomer actuators[14]

R. Sokhoyan, C. U. Hail, M. Y. Grajower, H. A. Atwater
Thomas J. Watson Laboratories of Applied Physics
California Institute of Technology
1200 E California blvd, Pasadena, California 91125, USA
E-mail: haa@caltech.edu
M. Foley
Department of Physics
California Institute of Technology
1200 E California blvd, Pasadena, California 91125, USA

DOI: 10.1002/lpor.202300980

 © 2024 Wiley-VCH GmbH

and microelectromechanical systems[15] to demonstrate adaptive metalenses. Prior research has demonstrated thermo-optically tunable Si nonlocal metasurfaces operating at near-infrared wavelengths.[16] These works,[14–16] however, do not allow for arbitrary wavefront reconfiguration of the transmitted light.

Several designs for dynamically tunable transmissive metasurfaces have been proposed using field effect control of the transmission phase[17] to dynamically shape the transmitted light wavefront but reported low optical efficiencies (<0.07%), limiting their use in practical applications. Recent theoretical work[18] has also demonstrated an all-dielectric transmissive metasurface which uses carrier injection in Si to realize subwavelength phase control in transmission as well as dynamic wavefront shaping. The optical efficiency of the reported metasurface is ≈65%. The maximal phase shift reported for 1D phase gradients was 215°, for an assumed refractive index of silicon $\Delta n \sim 0.01$.[18] Inverse design offers the prospect for high-directivity beam steering using all-dielectric transmissive metasurfaces, such as those based on reorientation of liquid crystal molecules.[19] It has been shown[20] that the optical anisotropy of the active liquid crystal medium surrounding the metasurface can be used to achieve large phase modulation in transmission while maintaining an optical efficiency of ≈100%. Prior research[21] has also used the concept of congener dipoles to develop a dynamic phase-change metasurface design that enables transmissive phase modulation covering over 240° while maintaining transmittance exceeding 80%. These recent theoretical studies,[20,21] however, do not assess wavefront shaping capabilities of the designed high-efficiency metasurfaces. Prior research[22] has also reported a thermo-optically reconfigurable metalens, which enables a continuous tunability of its focal length from 165 to 135 μm when the metalens temperature is increased from 20 to 260 °C. In our work, we use high quality factor subwavelength resonators as metasurface building blocks that enables achieving dynamically tunable optical response upon modest modulation of the external stimulus.

In the last few years, all-dielectric passive metasurfaces exhibiting high quality factors have been explored by researchers.[23] A number of prominent works have been exploring the potential of non-local metasurfaces.[24] For example, all-dielectric metasurfaces supporting delocalized photonic bound states in the continuum (BICs) have been demonstrated to show narrow-bandwidth resonances where a large electric field enhancement is observed.[23,25] In addition to structures that support delocalized modes, individual subwavelength dielectric resonators can support so-called quasi-BIC modes, also referred to as supercavity modes,[26] which exhibit moderately high quality factors and are weakly coupled to the radiative continuum. The high quality factor of the supercavity modes originates from interference of multiple localized modes supported by a resonator.[27] These distinct features have enabled use of quasi-BIC metasurfaces for numerous applications such as sensing[28] and harmonic generation.[29] Quasi-BIC mode subwavelength nanolasers have also been realized.[30] Quasi-BIC modes supported by an individual cylinder, however, cannot be efficiently excited by a normally incident linearly polarized light, and azimuthally polarized excitation is required.[26] For transmissive metasurfaces, normal incidence illumination with linearly polarized light is important for metasurface integration with chip-scale light sources. Notably, addition of an appropriately spaced back reflector to a cylinder array enables excitation of array quasi-BIC modes with normally incident light,[31] but a back reflector precludes their use for transmissive metasurfaces. Excitation of quasi-BIC (or, equivalently, supercavity) modes by a normally incident linearly polarized plane wave using a single high-index rectangular parallelepiped has also been reported.[32]

Here, we develop all-dielectric high-Q metasurface designs for dynamic beam switching or beam steering in transmission mode, utilizing the modest refractive index modulation achievable by thermo-optic modulation of amorphous Si (a-Si) with assumed index modulation ranging between $\Delta n = 0.0026$ to $\Delta n = 0.01$. Prior research[33] has theoretically demonstrated a high-Q beam steering active metasurface, which utilizes lithium niobate as an active material. The designed metasurface, [33] however, operates in reflection. Our *transmissive* active metasurface operates at near infrared wavelengths and can be excited by a normally incident linearly polarized light, exploiting either a high-Q mode or lower-Q modes supported by an individual a-Si rectangular parallelepiped (hereafter, for brevity, referred to as a square pillar). The spectral line shape of the high-Q mode at resonance can be "inverted" from exhibiting a dip in transmission to exhibiting a transmission peak by including a Si substrate separated from the square pillar by a silica (SiO_2) layer of appropriately chosen thickness. Notably, the resonances discussed in our work also exhibit large (≈300°) transmitted light phase spectral variation near resonance, which is a prerequisite for dynamically tunable phase shifts. We explore how refractive index modulation of modes of individual a-Si pillars can sculp the transmitted light wavefront both in the near and far field. Finally, we report designs for physically realizable interconnect architectures to enable dynamic beam steering via thermo-optic modulation.

2. Results and Discussion

Our metasurface motif consists of an array of a-Si rectangular pillars on an SiO_2 substrate (**Figure 1**a and b). We consider metasurface illumination by a linearly polarized (*x*-polarized) plane wave from within the SiO_2 substrate, and study phase and amplitude characteristics of the transmitted light. We find that this metasurface unit cell supports a high-Q optical mode for geometrical parameters $h = 860$ nm and $l = w = 963$ nm (see Figure 1b and c), and a metasurface period of $P_x = P_y = 1425$ nm. The refractive indices of a-Si and SiO_2 are taken as 3.734[34] and 1.44, respectively. The Q-factor of the supported mode is $Q = 9800$, as determined by fitting the transmittance spectrum with Fano form lineshape (Supporting Information, Part 1). The observed transmittance dip is accompanied by a broad spectral feature in the transmitted light phase (Figure 1c), indicating that this unit cell motif can permit design of metasurface phase gradients either via geometric tuning or an external active control.

To gain further insight about the high-Q mode, we investigate its spatial mode profile (see Figure 1d and e and Supporting Information, Part 2). Figure 1d indicates that in the *x*-direction, the electric field is tightly confined within the resonator and is enhanced by a factor of almost 80. While the largest electric field enhancement is inside the a-Si resonator, we also observe a more modest enhancement of the electric field below and above the a-Si pillar. On the other hand, in the *y*-*z* plane, which

© 2024 Wiley-VCH GmbH

18638899, 2024, 6, Downloaded from https://onlinelibrary.wiley.com/doi/10.1002/lpor.202300980 by California Institute Of Technology, Wiley Online Library on [15/10/2026]. See the Terms and Conditions (https://onlinelibrary.wiley.com/terms-and-conditions) on Wiley Online Library for rules of use; OA articles are governed by the applicable Creative Commons License

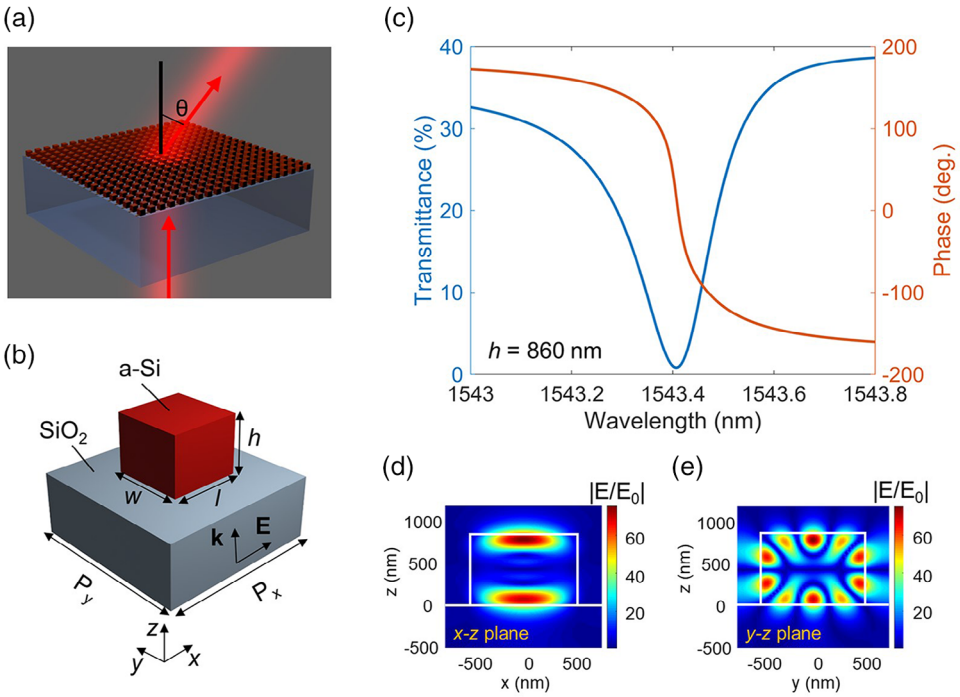


Figure 1. All-dielectric high-Q metasurfaces. a) Schematic of a transmissive metasurface, which consists of an array of amorphous a-Si rectangular pillars on an SiO_2 substrate. b) Schematic of a unit cell of a transmissive metasurface. c) Transmittance and phase spectra of the metasurface depicted in a). In c), the assumed geometrical parameters are as follows: the pillar height is $h = 860$ nm, and the pillar length l and width w are $l = w = 963$ nm. The metasurface period is $P_x = P_y = 1425$ nm. The a-Si resonators are illuminated by an x-polarized light from within the substrate. d) and e) show spatial distribution of the electric field amplitude in the metasurface unit cell in x-z and y-z planes, respectively. E_0 denotes the amplitude of the impinging electric field. Both in d) and e), the considered cross-section in which the electric field is calculated traverses the center of the a-Si resonator.

is perpendicular to the polarization of the incoming light, we observe a more complex electric field distribution where the only non-zero component is E_x (Figure 1e). In the y direction, a non-negligible electric field enhancement is observed between neighboring metasurface unit cells, which could be an indication of significant inter-resonator near-field coupling in the direction perpendicular to the incoming electric field. We find that this inter-resonator coupling has broad implications for comprehensive transmitted light wavefront control.

As a next step, we explore how the transmittance characteristics vary with the height of the square a-Si pillars while the width is kept fixed (**Figure 2**a). We observe that both the resonance lineshape and linewidth change upon increasing the pillar height (Figure 2b and c). At certain pillar heights, we observe asymmetric resonance lineshapes indicative of Fano resonances, namely a high-Q mode coupled to a broader mode or a "continuum" of modes. By fitting transmittance spectra to Fano resonance lineshapes, we obtained the dependence of the resonance quality factor and the Fano phase on the pillar height (see Supporting Information, Part 1). Notably, the Fano phase characterizes the phase difference between the narrow and broad resonant modes. We observe that the quality factor of the resonance increases with the pillar height, and peaks at $h = 860$ nm (Figure 2b), with a value of ≈9800. At a pillar height corresponding to the maximal Q-factor, the Fano phase passes through 90° (thus, the Fano asymmetry parameter is zero), indicating a symmetric quasi-Lorentzian lineshape. Interestingly, if we remove the substrate and consider an array of a-Si pillars suspended in free space, Q-factor can be as high as 221000 (see Supporting Information, Part 3). It may be possible to achieve even higher quality factors in free space by even more systematic variation of the pillar height. When changing the metasurface period, we observe that for periods exceeding 1300 nm, the spectral position of the resonance does not change significantly when increasing the metasurface period (Supporting Information, Part 4).

We also examine the spectral behavior of the transmitted light phase, which is of importance for metasurface applications. When the pillar height is below 860 nm ($h \leq 860$ nm), we observe that the phase of the transmitted light spans almost 360° when varying the wavelength of the transmitted light. On the other hand, when $h > 860$ nm, we observe an abrupt change in the spectral characteristics of the transmitted light (see Supporting Information, Part 5). For example, at a pillar height of $h =$ 870 nm, the phase spans only 40° (as a function of wavelength). Interestingly, for $h > 860$ nm, the phase variation is limited despite a high quality factor. Thus, we find that the pillar height should be below 860 nm for wavefront shaping applications.

We compare the optical mode supported by a pillar in an array to the mode of a single isolated pillar (Supporting Information, Part 5). An isolated subwavelength pillar on an SiO_2 substrate supports a high-Q mode with a Q-factor of 676, and the high-Q mode profile is identical to that observed in the array configuration (Figure 1e). For an isolated a-Si pillar in free space, the Q-factor of this mode exceeds 1000, whereas, for an a-Si resonator on a substrate, the Q-factor is reduced due to mode leakage into the substrate. Scattering cross-section calculations indicate that,

© 2024 Wiley-VCH GmbH

18638899, 2024, 6, Downloaded from https://onlinelibrary.wiley.com/doi/10.1002/lpor.202300980 by California Institute Of Technology, Wiley Online Library on [15/10/2026]. See the Terms and Conditions (https://onlinelibrary.wiley.com/terms-and-conditions) on Wiley Online Library for rules of use; OA articles are governed by the applicable Creative Commons License

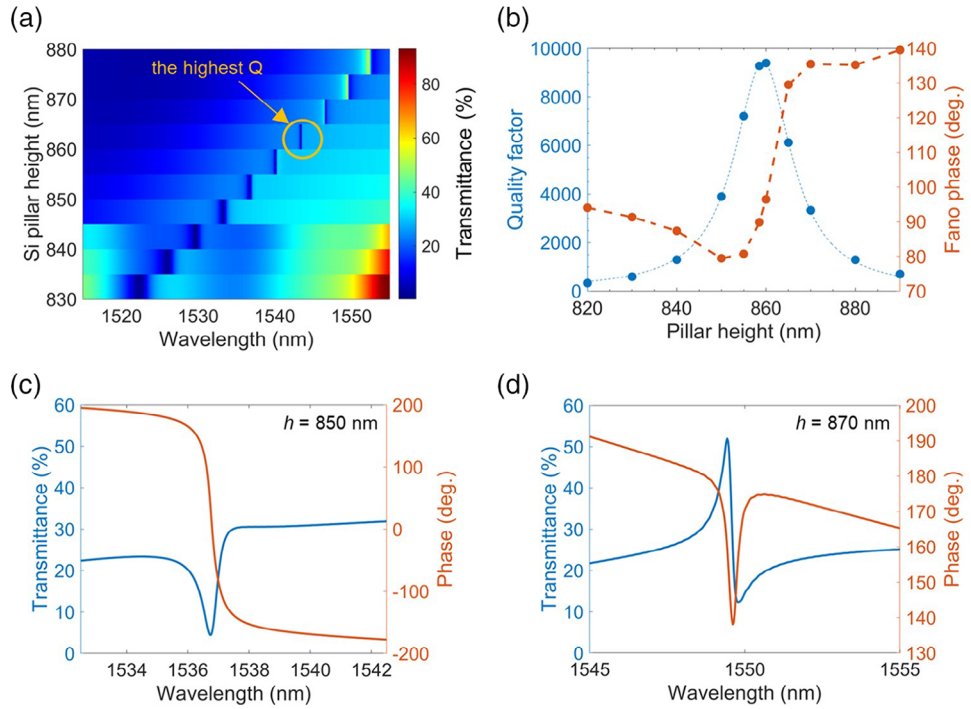


Figure 2. Dependence of the properties of the high-Q mode on the height of the a-Si square pillar. Transmittance a) as a function of wavelength and the a-Si pillar height h. b) Quality factor and Fano phase of the designed high-Q mode a function of the a-Si pillar height h. c) and d) show transmittance and phase as a function of wavelength for the a-Si pillar heights of $h = 850$ nm and $h = 870$ nm, respectively.

besides the high-Q mode, the isolated Si pillar also supports two lower-Q modes (Supporting Information, Part 5). When comparing isolated pillar mode profiles with mode profiles of a pillar in an array, we observe evidence of nonlocality for one of the lower-Q modes since its field profile is not observed in the isolated resonator (cf. Supporting Information, Part 5 and Part 3).

We investigate the dependence of the spectral position of the resonance on the metasurface period (see Figures S8 and S9, Supporting Information). We observe that changing the metasurface period does not significantly affect the spectral position of the high-Q resonance. Next, we consider metasurfaces with a finite number of metasurface elements in either the x or y direction (Supporting Information, Part 8). We observe that for 20 metasurface periods, the quality factor of the mode converges with the quality factor of the infinite metasurface array. Note that in the case of delocalized resonances, such as guided mode resonances, the effect of the finite grating size becomes negligible when the number of the grating periods approaches the quality factor of the resonance.[35] In our case, this would correspond to thousands of grating periods. These observations lead us to the conclusion that the high-Q mode reported in our work is quasi-local.

One shortcoming of this metasurface motif is that large phase variation is accompanied by low transmittance, and operating at the transmittance dip wavelength would result in low metasurface optical efficiency. A design modification that enables high Q-factor modes to be supported with large phase variation at a transmittance peak rather than a transmittance dip would be highly desirable. We find that the metasurface unit cell design shown in **Figure** 3a, with a crystalline silicon (c-Si) substrate and a SiO_2 spacer, enables these criteria to be achieved. The length and width of the a-Si pillar are as in our original design ($l = w = 963$ nm), but the height of the a-Si resonator has been slightly reduced to $h = 845$ nm, since considering taller pillars compromises variation of phase as a function of wavelength. The metasurface period is now chosen as $P_x = 1520$ nm and $P_y = 1425$ nm. Increasing the metasurface period in the x-direction to $P_x = 1520$ nm reduces the near-field coupling between the neighboring metasurface unit cells. The spectral shape of the transmittance can be controlled by changing the thickness of the SiO_2 spacer. We find, for example, that an SiO_2 spacer thickness of $d = 1450$ nm yields a large phase variation with wavelength accompanied by a transmittance peak of 37% (Figure 3b and Supporting Information, Part 6).

The electric field profiles for a modified unit cell (Figure 3a) exhibit mode leakage into the SiO_2 spacer (Supporting Information, Part 6). Both E_x and E_z components of the electric field have nonzero values in the SiO_2 spacer layer, and the electric field enhancement in a-Si pillars can be as high as 120. In addition to seeing changes in transmission, when changing the thickness of the SiO_2 spacer d, we observe variations in both the mode quality factor and Fano phase (Figure 3c). By appropriately choosing the SiO_2 thickness d, we can tune the Fano phase over the range 0° to 140° (Fano phase is uniquely defined between 0° to 180°). This large variation of the Fano phase is indicative of comprehensive control of the resonant lineshape, exhibiting transmission dips, transmission peaks and asymmetric spectral shapes. Thus, by tailoring resonator mode leakage into the spacer layer, we modify the relative phase between the high-Q mode and the continuum, resulting in a change of the transmittance spectral lineshape.

© 2024 Wiley-VCH GmbH

18638899, 2024, 6, Downloaded from https://onlinelibrary.wiley.com/doi/10.1002/lpor.202300980 by California Institute Of Technology, Wiley Online Library on [15/10/2026]. See the Terms and Conditions (https://onlinelibrary.wiley.com/terms-and-conditions) on Wiley Online Library for rules of use; OA articles are governed by the applicable Creative Commons License

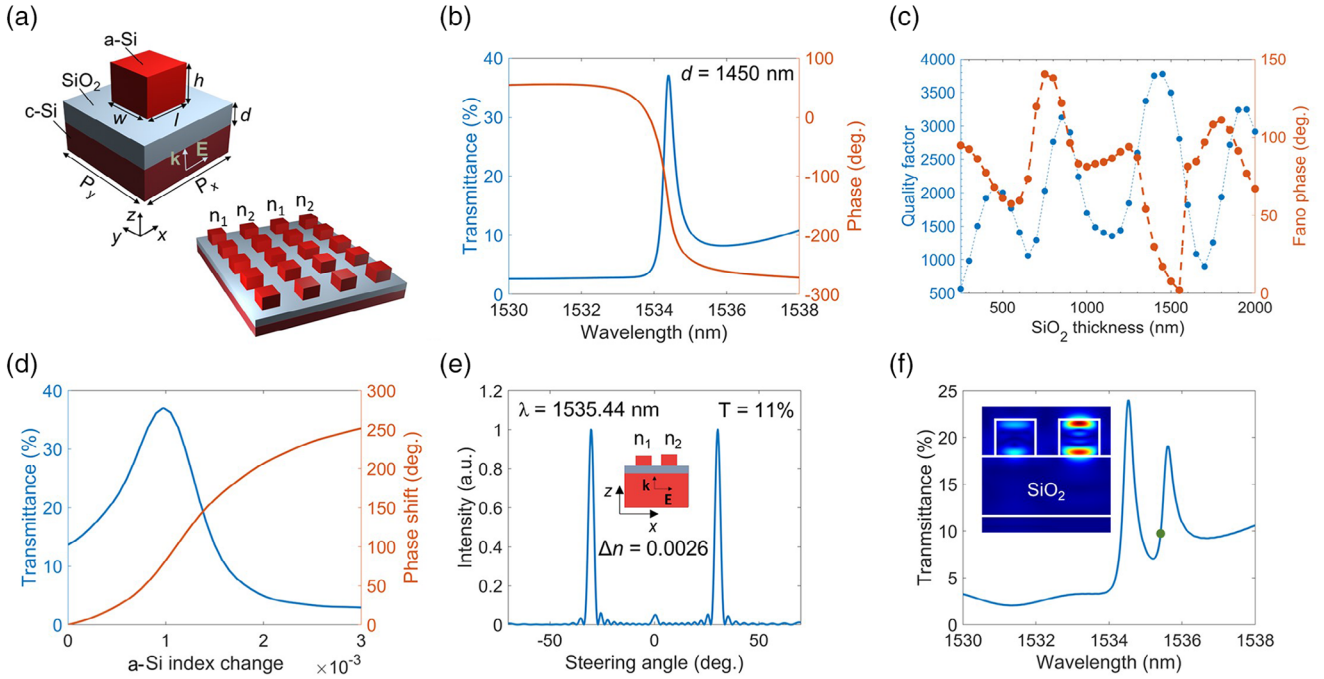


Figure 3. a) Schematic of a transmissive metasurface. In a) the top panel shows the schematic of the metasurface unit cell while the bottom panel shows the metasurface. The proposed alternative design consists of a c-Si substrate, a SiO_2 spacer, followed by an a-Si rectangular pillar. b) Transmittance and phase spectra of the metasurface with a unit cell shown in a). In b), we assume that the thickness of the SiO_2 spacer d is $d = 1450$ nm. The height, width, and length of the a-Si pillar are $h = 845$ nm, and $w = l = 963$ nm. The assumed period values are $P_x = 1520$ nm and $P_y = 1425$ nm. c) The resonance quality factor and Fano phase as a function of the SiO_2 thickness. d) Transmittance and phase shift as a function of the a-Si index change at a wavelength of $\lambda = 1534.8$ nm. e) Intensity of the electric field in the far field for a two-level phase grating with 10 grating periods when the index change between neighboring a-Si pillars is $\Delta n = 0.0026$. f) Overall transmittance of the two-level grating. In f), the green dot marks the transmittance at an operating wavelength of $\lambda = 1535.44$ nm. The inset of f) shows the spatial distribution of the electric field in the x-z cross-section of the unit cell. The considered x-z cross-section goes through the center of the a-Si pillars.

As a next step, we assess metasurface beam steering (Figure 3a). First, we consider the case in which all pillar refractive indices change by an equal amount Δn and calculate the phase shift and the transmittance as a function of the index change Δn at a given wavelength. Note the phase shift is defined as a difference between the phase of the transmitted light at $\Delta n \neq 0$ and at $\Delta n = 0$. Our calculations show that a modest refractive index change of $\Delta n = 3 \times 10^{-3}$ results in a phase shift of ≈250° (Figure 3d), which is sufficient to enable beam steering.

We consider the case of 1D beam steering where the phases of all metasurface elements along the y direction are identical while the phases of neighboring elements in the x direction differ. Calculations for periodic arrays of identical elements suggest that an index change that would yield a 180° phase shift between neighboring elements in the x direction can create a two-level phase grating and strongly suppress the zeroth order beam. However, our full wave simulations indicate that the index change value derived via this method is not optimal, as we obtain an unexpectedly large zeroth order beam. The observed low diffraction efficiency is due to non-negligible near-field coupling between neighboring metasurface elements. Our calculations indicate that an index change $\Delta n = 0.0026$ between neighboring rows of a-Si resonators at fixed operating wavelength of $\lambda = 1535.44$ nm can fully extinguish the zeroth order diffraction beam (Figure 3e). Interestingly, for these parameters ($\lambda = 1535.44$ nm, $\Delta n = 0.0026$), the predicted relative phase shift between light scattered by adjacent rows of pillars is only 107°, according to the simulations of periodic arrays of identical resonators. In principle, this phase should result in a non-negligible zeroth order beam (Supporting Information, Part 6). These results indicate that such a simple ansatz for optimal beam steering does not readily apply for these high-Q metasurfaces.

Metasurface optical efficiency is a key design parameter; we find that overall transmittance of the two-level phase grating is $T = 11\%$ (Figure 3e and f) which is significantly lower than the peak transmittance of ≈35% derived from the identical resonator array simulations (Figure S19, Supporting Information). The observed reduction in transmittance is due to the spectral shape of the resonance (Figure 3b). As seen in Figure 3b, the transmittance falls off abruptly when moving away from the resonant wavelength. When realizing a two-level grating, the resonant wavelength of every other metasurface element is shifted, resulting in the reduction of the overall transmittance at a given operating wavelength. The transmittance spectrum of the two-level phase grating exhibits two distinct peaks (Figure 3f). The near-field distribution of the electric field (see the inset of Figure 3f) indicates that at a given operating wavelength, the relative electric field enhancement in neighboring a-Si rectangular pillars differs quite significantly. The optimal operating wavelength, which is marked by a green dot in Figure 3f, is located between the two resonant peak wavelengths resulting in a lower overall transmittance. To ensure wavefront shaping with higher optical efficiency,

© 2024 Wiley-VCH GmbH

18638899, 2024, 6, Downloaded from https://onlinelibrary.wiley.com/doi/10.1002/lpor.202300980 by California Institute Of Technology, Wiley Online Library on [15/10/2026]. See the Terms and Conditions (https://onlinelibrary.wiley.com/terms-and-conditions) on Wiley Online Library for rules of use; OA articles are governed by the applicable Creative Commons License

one needs to ensure that the transmittance stays above a certain minimal value when spectrally moving away from the resonance.

The design of high-Q dynamic beam steering metasurfaces has two major challenges: i) One cannot use intuitive phase profile to steer the beam with a high steering efficiency, and the optimal beam steering conditions have to be identified via full wave simulations; ii) diffractive switching occurs only in one direction due to very significant inter-emitter near-field coupling in the direction perpendicular to the polarization of the incoming electric field (y-direction). Hence, it would be desirable to identify optical modes which enable 2D beam steering.[36]

Besides the high-Q mode, several lower-Q modes are supported with quality factors of ≈200 (Supporting Information, Parts 3 and 4). The metasurface (Figure 1) with a-Si rectangular pillar height, width, and length of h = 845 nm, and $w = l$ = 963 nm, respectively, and the period of $P_x = P_y$ = 1500 nm, exhibits a relatively low-Q photonic mode at a wavelength of 1583 nm (**Figure 4a**). As seen in Figure 4a, the resonant dip observed at a wavelength of 1583 nm is also accompanied by a large spectral variation of the phase. When changing the refractive index of a-Si pillars by $\Delta n = 0.01$ everywhere in the metasurface, we observe a dynamically tunable phase shift of ≈285° (Figure 4b), which is large enough to enable dynamical beam steering.

Next, we investigate whether the lower-Q mode can be used for dynamic beam steering, in two configurations: i) when the beam is steered in the direction perpendicular to the polarization of the incoming electric field (transverse electric or TE case); ii) when the steering direction is aligned with the polarization of the incoming light (transverse magnetic or TM case). First, we consider the case of a two- level phase grating and assume that the a-Si index change between neighboring element rows is Δn = 0.0048 (for schematic of a grating period see insets of Figure 4c and d). At Δn = 0.0048, neighboring metasurface rows are expected to exhibit a phase difference of 180° at a wavelength of λ = 1583.85 nm (Figure 4b). Thus, we expect a near complete suppression of the specularly transmitted beam. However, our full wave simulations show significant transmission at normal incidence, for two reasons: i) near-field coupling between neighboring metasurface elements, ii) the difference in scattered light amplitude from neighboring elements.[37]

To fully suppress the normally transmitted beam at an operating wavelength of λ = 1583.85 nm, we developed an optimization procedure for the pillar refractive indices to maximize the diffraction efficiency of a desired order (see Methods), resulting in full suppression of the zeroth diffraction order at an operating wavelength of λ = 1583.85 nm for both TE and TM polarizations of the incoming light (Figure 4c and d). In the case of the TE polarization, the optimized refractive index of the one of the a-Si pillars within the grating period retained its original value (n_1 = 3.734), and the refractive index difference Δn between neighboring a-Si pillars is Δn = 0.0055, which yields a phase shift of 200° (see Figure 4b), which is close to the originally chosen phase shift of 180°. In the case of the TM polarization, the optimization procedure yielded a-Si refractive indices: n_1 = 3.7353 and n_2 = 3.7440. The corresponding phase difference for adjacent a-Si pillars is 270 °, which significantly deviates from the original value of 180°. For TM polarization, full suppression of the zeroth diffraction order occurs for a phase profile which significantly differs from the optimal phase shift uncoupled resonator array, indicating that inter-element near-field coupling is more significant for TM than TE polarization.

Although we observed diffractive switching of a two-level phase grating, this analysis does not clarify whether intermediate steering angles are possible using a blazed grating-type design approach. In the case of TM polarization, using three- and four-level blazed grating phase profiles, we did not obtain a highly directional beam owing to near-field coupling between neighboring metasurface elements. However, for TE polarization, we demonstrated beam steering to angles of 20.6° and 15.2° with reasonable diffraction efficiencies. To steer a beam to a polar angle of 20.6°, we use Figure 4b to construct a phase a three-level phase profile with relative phase between elements of 0°, 120°, 240°, respectively, resulting in beam steering with a diffraction efficiency of 60% at an operating wavelength of λ = 1583.85 nm (Figure 4g). To steer the beam to a polar angle of 15.2°, a phase profile of 0°, 90°, 180°, 270° was constructed, resulting in a diffraction efficiency of 38% at an operating wavelength of λ = 1583.85 nm and 46% at λ = 1584.16 nm. To improve the diffraction efficiency at λ = 1583.85 nm, we performed a full wave optimization procedure, yielding a diffraction efficiency of 52% (Figure 4h), with a-Si refractive indices: n_1 = 3.7340, n_2 = 3.7358, n_3 = 3.7386 n_4 = 3.7417. Thus, for TE-polarized incident light, our metasurface can steer the beam to intermediate angles between 0° and 20.6°.

The overall transmittance of the four-level phase grating is higher as compared with the overall transmittance of the three-level phase grating (cf. Figure 4h and g). This is due to the fact that the transmission amplitude values of the four-level phase grating are on average higher as compared with the transmission amplitude values of the three-level phase grating (Figure 4b).

Having determined that both high- and lower-Q modes can be used for transmitted light wavefront manipulation, we seek a feasible design to enable refractive index variation and dynamic beam switching, by refractive index modulation of a-Si using the thermo-optic effect.[13,22,38] To selectively heat rows of a-Si pillars, we introduce a-Si electrodes and connect the pillars in series (**Figure 5a** and b). In our design, we place a-Si pillars on SiO_2 pedestals to limit thermal crosstalk between neighboring pillars. Fabrication entails first pattering a-Si on an SiO_2 spacer followed by hydrofluoric acid wet etching of the SiO_2 spacer into pillars on a c-Si substrate.

Figure 5a and b illustrate this design - the top and bottom 50 nm-thick a-Si layers are doped, and a voltage is applied to the top and bottom layer resulting in current flow between the electrodes through the lightly doped a-Si layer (see Figure 5b). The induced current raises the temperature T of a-Si pillars by Joule heating, with modified a-Si refractive index $n(T) = n_{Si} + \Delta n(\Delta T)$. For silicon, a temperature change of ΔT = 10 K changes the refractive index by Δn = 0.00239. [39] Dynamic beam switching using a higher-Q mode is possible with refractive index difference as low as Δn = 0.0026, corresponding to a relative temperature difference of ≈11 K. For beam switching with lower-Q modes, a refractive index difference of Δn = 0.006 is required, corresponding to a relative temperature difference of ΔT = 25 K. These numerical estimates suggest our metasurface can potentially enable beam steering with quite modest temperature differences.

To construct a desired transmitted light phase profile, we can heat individual rows of pillars to different temperatures. For the high-Q mode, diffractive switching with a two-level phase grating

© 2024 Wiley-VCH GmbH

18638899, 2024, 6, Downloaded from https://onlinelibrary.wiley.com/doi/10.1002/lpor.202300980 by California Institute Of Technology, Wiley Online Library on [15/10/2026]. See the Terms and Conditions (https://onlinelibrary.wiley.com/terms-and-conditions) on Wiley Online Library for rules of use; OA articles are governed by the applicable Creative Commons License

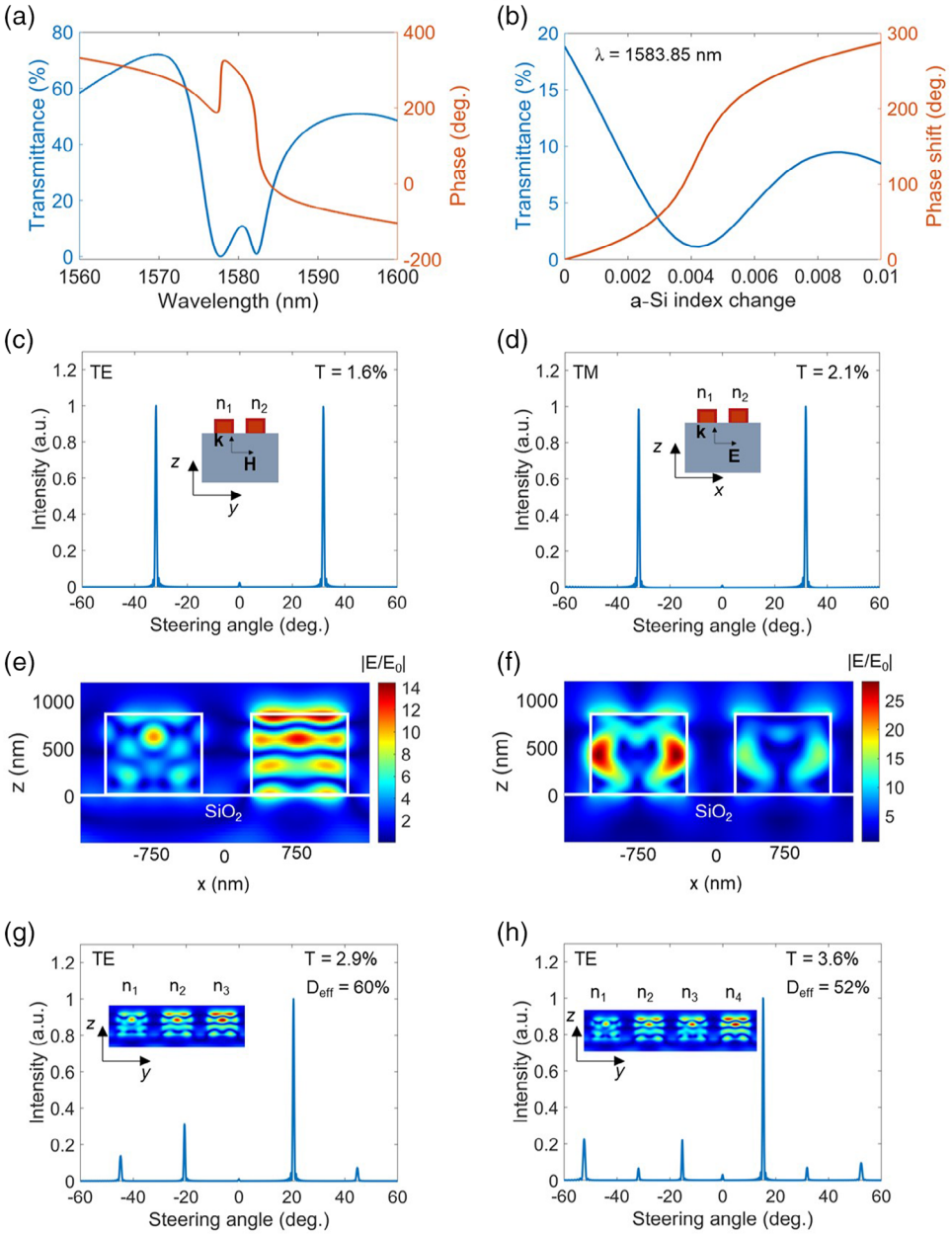


Figure 4. Beam steering using the lower-Q mode. a) Transmittance and phase spectra of the metasurface with a unit cell shown in Figure 1b). In a), the assumed metasurface period values are $P_x = 1500$ nm and $P_y = 1500$ nm. The assumed geometrical parameters are as follows: the pillar height is $h = 845$ nm, and the pillar length and width are $l = w = 963$ nm. b) Transmittance and phase shift as a function of the a-Si index change at a wavelength of $\lambda = 1583.85$ nm. c) Intensity of the electric field in the far field as a function of the polar (steering) angle for a two-level phase grating when the incoming electric field is polarized perpendicular to the steering direction (TE polarization). d) Intensity of the electric field in the far field for a two-level phase grating when the incoming electric field is parallel to the steering direction (TM polarization). e) Near-filed electric field distribution in the two-level phase grating depicted in the inset of c), which corresponds to the case of the TE polarization. f) Near-filed electric field distribution in the two-level phase grating depicted in the inset d), which corresponds to the case of the TM polarization. In e) and f), E_0 denotes the amplitude of the impinging electric field. g) and h) plot the intensity of the electric field in the far field as a function of the steering angle in the cases of three-level and four-level phase gratings, respectively. g) and h) correspond to the case of the TE polarization. The insets of g) and h) show the near-field distribution of the electric field in each case. The overall transmittance values are specified in the insets of c), d), g), and h). The operating wavelength is $\lambda = 1583.85$ nm.

© 2024 Wiley-VCH GmbH

18638899, 2024, 6, Downloaded from https://onlinelibrary.wiley.com/doi/10.1002/lpor.202300980 by California Institute Of Technology, Wiley Online Library on [15/10/2026]. See the Terms and Conditions (https://onlinelibrary.wiley.com/terms-and-conditions) on Wiley Online Library for rules of use; OA articles are governed by the applicable Creative Commons License

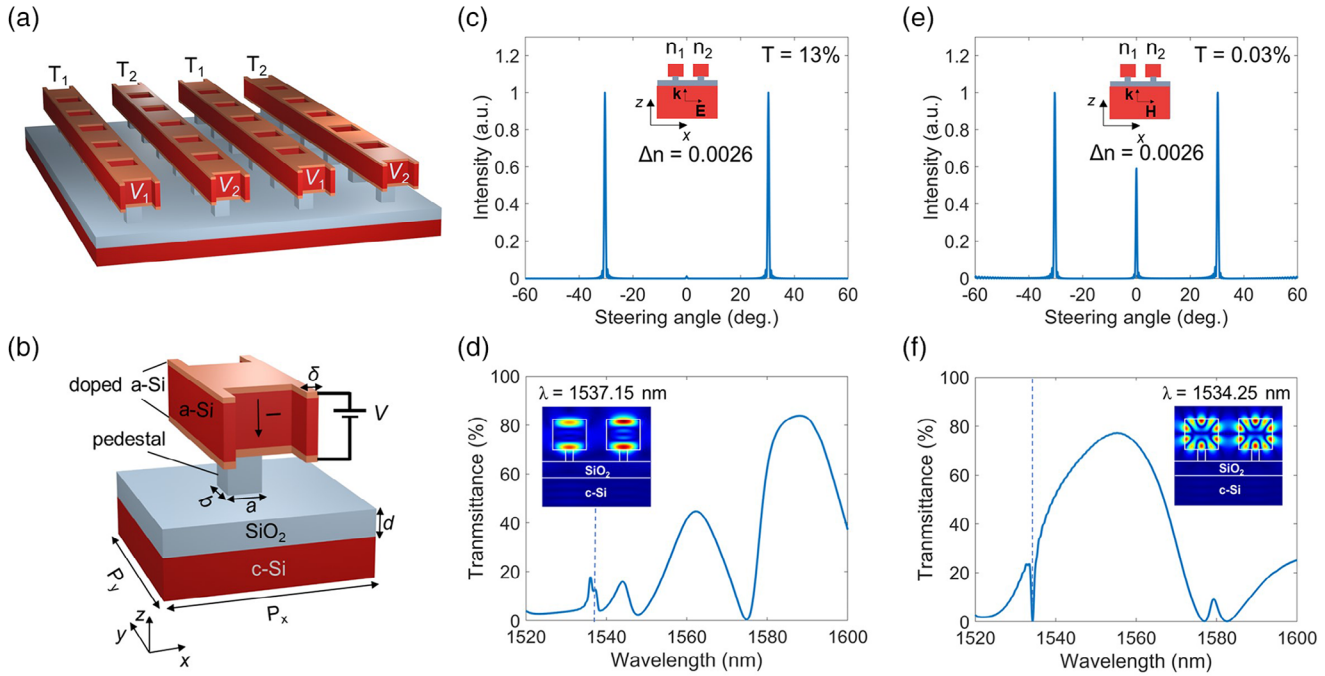


Figure 5. Thermo-optic beam switching using the high-Q mode with a realistic interconnect architecture. In a), schematic of the proposed metasurface. In b), schematic of the proposed metasurface unit cell. In a)-b), the square a-Si pillars are connected via a-Si bars. Each a-Si pillar is placed upon an SiO_2 pedestal to enhance thermal insulation between neighboring metasurface elements. The width and length of the pillar is $w = l = 963$ nm, the height of the pillar is $h = 850$ nm. The width of the bar is $\delta = 50$ nm, and the height of the bars is 850 nm. The SiO_2 pedestal has a shape of a rectangular pillar with a length and width $a = b = 200$ nm, and a height of 382 nm. The thickness of the planar SiO_2 spacer is $d = 380$ nm. The whole structure is built on an c-Si substrate. In c), the intensity of the electric field in the far field for a two-level phase grating when the incoming plane wave is *x* polarized. In c), the operating wavelength is $\lambda = 1537.15$ nm. In d), the overall transmittance spectrum corresponding the two-level phase grating studied in c). In e), the intensity of the electric field in the far field for a two-level phase grating when the incoming plane wave is *y* polarized. In e), the operating wavelength is $\lambda = 1534.25$ nm. In f), the overall transmittance spectrum corresponding the two-level phase grating studied in f). Insets of d) and f) show spatial distribution of the electric field in the *x*-*z* cross-section of the grating period at operating wavelengths in case of *x*- and *y*-polarized incoming light, respectively. The refractive index difference between neighboring metasurface elements is $\Delta n = 0.0026$.

can be realized by changing the temperature of every other metasurface pixel (i.e., electrically connected rows of metasurface elements) by 11 K ($\Delta n = 0.0026$). Heating to create a two-level phase grating, deflects the light to angles of $\theta = \pm 30°$ (Figure 5c and e). For an incident *x*-polarized electric field, this modest refractive index difference enables diffractive beam switching with a complete suppression of the zeroth diffraction order and an overall transmittance of $T = 13$ % (Figure 5c). We also observe diffractive beam switching for *y*-polarized incidence (Figure 5d) with a lower overall transmittance and at a different operating wavelength. For a-Si on an SiO_2 substrate, we only observed diffractive switching for the high-Q mode when the steering direction aligned the incoming plane wave (TM) polarization. The a-Si electrodes and the SiO_2 pedestal serve to reduce near-field coupling of neighboring metasurface elements. Lower-Q modes are also capable of diffractive switching for both TE and TM polarized incidence, at different wavelengths.

We also performed a coupled electrical and thermal analysis (see Methods). To induce a diffraction grating analogous to the one in Figure 5a, we apply a voltage of $V_1 = 1.05$ V between top and bottom doped a-Si layers of one metasurface pixel while grounding each neighboring metasurface pixel ($V_2 = 0$ V) in a periodic array. **Figure** 6a illustrates the calculated current density in the silicon bars in one grating period. The largest current density and most significant heat generation occurs in the top and bottom doped a-Si layers of the connector bars. Figure 6b illustrates the steady state temperature distribution for one grating period for $V_1 = 1.05$ V and $V_2 = 0$ V, such that the temperatures of two adjacent metasurface pixels are $T_1 = 312.8$ K and $T_2 = 301.4$ K, respectively, yielding refractive index difference of $\Delta n = 0.0026$, assuming a thermo-optic coefficient of 2.3×10^{-4} K^{-1}.[39] The power density required to maintain this temperature difference in steady state is 1.62 μW μm^{-2}. The temperature distribution in the pillars and connectors is nearly uniform due to the high thermal conductivity of silicon, even though heating occurs predominantly in the connector bars. The largest temperature gradient occurs in the silicon oxide pedestal due to its large thermal resistance, which greatly reduces the thermal crosstalk between adjacent rows. To assess metasurface dynamic performance, we carried out transient electrical and thermal simulations of dynamic thermal switching between the two pixels comprising one grating period. A response time of 7.3 μs is obtained for a square wave voltage profile (see Figure 6c), indicating that thermo-optic switching is possible at frequencies up to 140 kHz.

Finally, we assess metasurface beam steering performance with realistic interconnects (Figure 5a) when a three-level phase profile (0°, 120°, 240°) is applied to the metasurface, for both lower-Q and high-Q modes under TM-polarized plane wave

© 2024 Wiley-VCH GmbH

18638899, 2024, 6, Downloaded from https://onlinelibrary.wiley.com/doi/10.1002/lpor.202300980 by California Institute Of Technology, Wiley Online Library on [15/10/2026]. See the Terms and Conditions (https://onlinelibrary.wiley.com/terms-and-conditions) on Wiley Online Library for rules of use; OA articles are governed by the applicable Creative Commons License

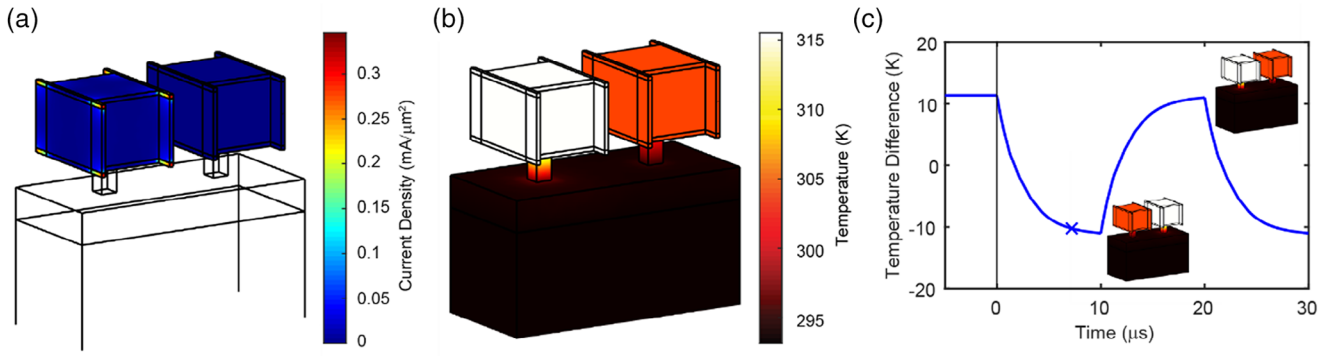


Figure 6. Electrical and thermal analysis of thermo-optic beam switching. a) Steady state spatial current density distribution in a thermo-optically controlled metasurface with $V_1 = 1.05$ and $V_2 = 0$ V. b) Steady–state spatial temperature distribution in a thermo-optically controlled metasurface with $V_1 = 1.05$ and $V_2 = 0$ V. c) Transient temperature difference between the two rows of a thermo-optically controlled metasurface when switching the voltage with a square wave of amplitude $V = 1.05$ V and a frequency of 100 kHz. The geometrical parameters are identical to the ones of the structure in Figure 5.

illumination. This phase profile yields a maximum diffraction efficiency of 35% for the lower-Q mode and 28% for the high-Q mode (see Supporting Information). Optimization (see Methods) of the a-Si pillar refractive indices resulted in a modest improvement of diffraction efficiencies. To further increase diffraction efficiency, we co-optimized the geometrical parameters of the structure and refractive indices of a-Si pillars (see Methods) enabling enhanced diffraction efficiencies of 54% and 69% for the lower-Q and the high-Q mode, respectively (see **Figure 7**).

3. Conclusions

In summary, all-dielectric dynamically tunable transmissive metasurfaces are achievable using high-Q resonances with Q-factors approaching 10 000. Appropriate design enables the metasurface to exhibit a transmittance *peak* (rather than a transmittance dip at the resonant wavelength for Q-factors of ≈3780 (Figure 3a). These high quality factors enable achieving beam steering at modest variations of the a-Si refractive index on the order of 10^{-3}, which is a unique advantage of the proposed design. Lower-Q modes can also be used for amplitude and phase modulation, but the required a-Si refractive index modulation is higher (up to 0.01) as compared with the case of high-Q mode. Thermo-optically active elements can be addressed using interconnects that do not perturb the resonator cavity modes, and both high-Q and lower-Q modes can realize thermo-optic beam switching, with switching times as low as 7.3 μs. For both high-Q and lower-Q modes, dynamic switching of both TE- and TM-polarized light is possible, although at different wavelengths. Using a three-level phase grating approach, we have shown that the metasurface with realistic interconnects is capable of dynamic beam steering, with diffraction efficiencies of 54% and 69% for lower Q and high-Q modes, respectively. Finally, we note that the optical efficiency of the proposed metasurface can be significantly enhanced by introducing a metallic back reflector and a SiO_2 spacer. The designed reflective metasurfaces may exhibit optical efficiencies >90% (Supporting Information, Part 10).

Thermo-optic effect is only one of the possible pathways for actively modulating the designed metasurface. Another interesting idea would be introducing a thin transparent conductive oxide (TCO) layer such as ITO[40] or cadmium oxide[41] underneath the a-Si pillars and using field effect modulation to actively control

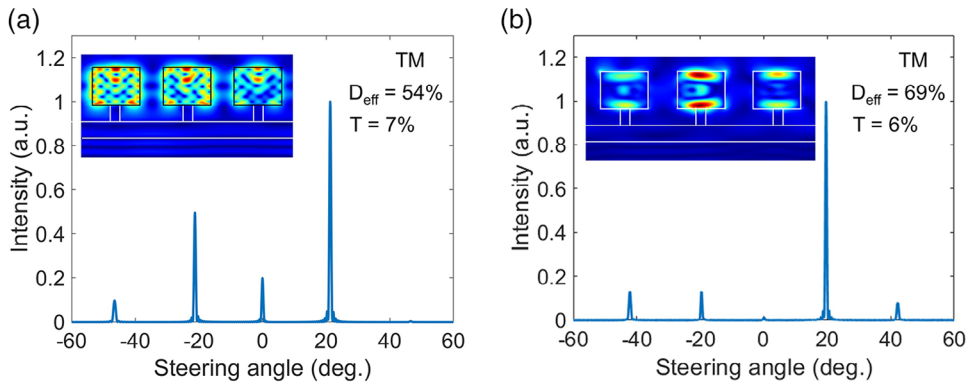


Figure 7. Thermo-optic three-level phase grating with a realistic interconnect architecture and optimized geometry. The incoming plane wave is TM-polarized. a) Intensity of the electric field in the far field for the case of the lower-Q mode. In a), the operating wavelength is $\lambda = 1567.1$ nm. b) Intensity of the electric field in the far field for the case of the high-Q mode. In b), the operating wavelength is $\lambda = 1531.3$ nm. The insets of a) and b) show the spatial distribution of the electric field in the *x-z* cross-section of the grating period at the operating wavelengths.

© 2024 Wiley-VCH GmbH

18638899, 2024, 6, Downloaded from https://onlinelibrary.wiley.com/doi/10.1002/lpor.202300980 by California Institute Of Technology, Wiley Online Library on [15/10/2026]. See the Terms and Conditions (https://onlinelibrary.wiley.com/terms-and-conditions) on Wiley Online Library for rules of use; OA articles are governed by the applicable Creative Commons License

the optical response of metasurface via gating. As shown in previous works, epsilon-near-zero transition in TCOs can be a useful mechanism for achieving phase modulation.[40,41] The second TCO layer can be added as a counter-electrode. Another interesting idea would be combining lossless electro-optic materials such as lithium niobate or JRD1 molecules embedded in a polymer, with high-Q metasurfaces as discussed in recent works.[33,42] In this case, Pockels effect in electro-optic materials will be used for achieving electrically tunable optical response.

4. Methods

Optical simulations were performed using the finite difference time domain method (FDTD Lumerical). In our optical simulations, a normally incident linearly polarized plane wave illuminates the metasurface from within the substrate (see Figures 1 and 2). When simulating an array of a-Si pillars, periodic boundary conditions are used in the x and y directions, and perfectly matched layers (PML) boundary condition is used in the z direction. When considering the behavior of an isolated pillar, PML boundary conditions are used at all simulation boundaries, and the simulation volume is $3 \times 3 \times 3$ μm^3. In our simulations the materials are assumed non-dispersive. The refractive indices of a-Si, SiO_2, and c-Si are taken as 3.734,[34] 1.44, 3.43, respectively. The effect of potential fabrication non-idealities on the metasurface performance is summarized in Supporting Information, Part 9. When considering realistic interconnect architectures to perform thermo-optic beam switching and thermo-optic beam steering, we assume the complex refractive index of the doped a-Si layers is given as $n = 3.734+0.0013$ i, which corresponds to the carrier density of 6×10^{18} cm^{-3} in the case of the n-doped Si layer and the carrier density of 10^{19} cm^{-3} in case of the p-doped Si layer. [43] Complex refractive index of the lightly doped Si core is $n = 3.734+0.000025$ i, which corresponds to the carrier density of 3.2×10^{17} cm^{-3} of the n-doped Si.[43] In simulations used to generate Figures 1 and 2, the assumed mesh in the z-direction is 5 nm while the mesh in the x- and y-directions is set to 20 nm. In our beam switching and beam steering simulations, the mesh in the x-, y-, and z-directions is set to 20 nm. When performing the near to far field projection in Figure 3, we assume that the number of metasurface elements in the x-direction is 20, while for the near to far field projection in Figures 4, 5, and 7, the number of assumed metasurface elements in the x-direction is 100.

To optimize diffraction efficiencies, we used MATLAB to drive a multi-variable nonlinear optimization in FDTD via Lumerical's Automation Application Programming Interface (API). When performing the optimization, we used the sequential quadratic programming method and used the inverse of the maximal diffraction efficiency as a figure of merit. The phase profile was assumed periodic, and the geometry and the refractive indices of the structure within a period were varied. When optimizing diffraction efficiencies in Figure 4, only refractive indices of a-Si pillars were varied so that the maximal assumed index change was $\Delta n = 0.01$. When optimizing diffraction efficiencies of the structure with realistic interconnects (Figure 7) we run a series of optimization runs. First, we co-optimized only refractive indices of the metasurface elements. In the next step, we fixed the refractive index of the first metasurface element n_1 and co-optimized the structure height and the refractive indices of the two remaining metasurface elements. Next, we co-optimized the P_y period (or P_x period) of the structure and refractive indices of the second and third metasurface element while keeping the refractive index of the first metasurface element fixed. As a final optimization step, we re-optimized the refractive indices of all three metasurface elements. In the case of the lower-Q mode, the optimization yields the following values for the refractive indices of the Si pillars and the geometrical parameters of the structure: $n_1 = 3.73416$, $n_2 = 3.738299$, $n_3 = 3.73778$, $P_x = 1440$ nm, $P_y = 1440$ nm, and $h = 840.75$ nm, and the observed diffraction efficiency $D_{eff} = 54\%$ (Figure 7a). In the case of the high-Q mode, the obtained parameter values are as follows: $n_1 = 3.73416$, $n_2 = 3.7383$, $n_3 = 3.744$, $P_x = 1520$ nm, $P_y = 1495.92$ nm, and $h = 841.207$ nm, and the resulting diffraction efficiency $D_{eff} = 69\%$ (Figure 7b). When optimizing the beam steering performance of the high-Q mode, we observed that co-optimizing the pillar height and the two of the refractive indices has enabled us increasing the diffraction efficiency from 36% to 53%. As a result of the optimization, the a-Si pillar height was reduced from 850 to 841 nm. Next, co-optimizing the period P_y and the two of the refractive indices has enabled increasing the diffraction efficiency to 69%. As a result of the optimization, the period P_y was increased from 1425 nm to 1440 nm.

3D electrical and thermal simulations were performed using finite element method (COMSOL Multiphysics). In our electrical simulations, we assume that, in the metasurface unit cell, the top and bottom 50 nm of a-Si are n-doped with assumed carrier density of 6×10^{18} cm^{-3}. The carrier density of the lightly doped core is taken to be 3.2×10^{17} cm^{-3}. First, we use electrical solver to obtain the volumetric heat source distribution due to Joule heating. As a next step, we use a thermal solver to obtain the temperature distribution. Our thermal simulations account for heat conduction and convection. We assume that the top of the metasurface is cooled via natural convection with a heat transfer coefficient of $h = 5$ W m^{-2} K. We also assume that the temperature at the bottom of the substrate, 50 mm from the metasurface is fixed to 298 K with an external heat sink. The assumed ambient temperature is also 298 K. When performing thermal simulations, we use periodic boundary conditions in the x and y directions.

Supporting Information

Supporting Information is available from the Wiley Online Library or from the author.

Acknowledgements

This work was supported by grant #FA9550-18-1-0354 from Air Force Office of Scientific Research as well as the Meta-Imaging MURI grant #FA9550-21-1-0312 from Air Force Office of Scientific Research. C.U.H. also acknowledges support from the Swiss National Science Foundation through the Early Postdoc Mobility Fellowship grant #P2EZP2_191880 and the Postdoc Mobility grant #P500PT_214452.

Conflict of Interest

The authors declare no conflict of interest.

© 2024 Wiley-VCH GmbH

18638899, 2024, 6, Downloaded from https://onlinelibrary.wiley.com/doi/10.1002/lpor.202300980 by California Institute Of Technology, Wiley Online Library on [15/10/2026]. See the Terms and Conditions (https://onlinelibrary.wiley.com/terms-and-conditions) on Wiley Online Library for rules of use; OA articles are governed by the applicable Creative Commons License

Author Contributions

R.S., H.A.A., and C.U.H. conceived the project. R.S. designed the metasurface and performed optical simulations. M.F. extracted Q-factors and Fano phase from the simulated transmittance spectra and performed a finite array analysis. C.U.H. performed electrical and thermal simulations and devised strategies minimizing thermal crosstalk. R.S. and M.Y.G. performed the full wave optimization. C.U.H., M.Y.G., and M.F contributed to the discussion of the results. R.S. wrote the manuscript with inputs from other authors. H.A.A supervised all aspects of the project.

Data Availability Statement

The data that support the findings of this study are available from the corresponding author upon reasonable request.

Keywords

active metasurfaces, beam steering, Fano asymmetry parameter, high-Q, thermo-optic, transmissive metasurfaces

Received: October 1, 2023
Revised: January 10, 2024
Published online: February 8, 2024

[1] G. K. Shirmanesh, R. Sokhoyan, P. C. Wu, H. A. Atwater, *ACS Nano* **2020**,*14*, 6912.
[2] S.-Q. Li, X. Xu, R. Maruthiyodan Veetil, V. Valuckas, R. Paniagua-Domínguez, I. Kuznetsov Arseniy, *Science* **2019**,*364*, 1087.
[3] a) A. M. Shaltout, V. M. Shalaev, M. L. Brongersma, *Science* **2019**,*364*, eaat3100; b) C. U. Hail, A.-K. U. Michel, D. Poulikakos, H. Eghlidi, *Adv. Opt. Mater.* **2019**,*7*, 1801786.
[4] P. Thureja, R. Sokhoyan, C. U. Hail, J. Sisler, M. Foley, M. Y. Grajower, H. A. Atwater, *Nanophotonics* **2022**,*11*, 3745.
[5] J. Park, B. G. Jeong, S. I. Kim, D. Lee, J. Kim, C. Shin, C. B. Lee, T. Otsuka, J. Kyoung, S. Kim, K.-Y. Yang, Y.-Y. Park, J. Lee, I. Hwang, J. Jang, S. H. Song, M. L. Brongersma, K. Ha, S.-W. Hwang, H. Choo, B. L. Choi, *Nat. Nanotechnol.* **2021**,*16*, 69.
[6] Y.-Y. Xie, P.-N. Ni, Q.-H. Wang, Q. Kan, G. Briere, P.-P. Chen, Z.-Z. Zhao, A. Delga, H.-R. Ren, H.-D. Chen, C. Xu, P. Genevet, *Nat. Nanotechnol.* **2020**,*15*, 125.
[7] K. Hirose, Y. Liang, Y. Kurosaka, A. Watanabe, T. Sugiyama, S. Noda, *Nat. Photonics* **2014**,*8*, 406.
[8] Y. Lee, J. Yun, S.-J. Kim, M. Seo, S. In, H.-D. Jeong, S.-Y. Lee, N. Park, T. D. Chung, B. Lee, *Adv. Opt. Mater.* **2020**,*8*, 2001256.
[9] A. Howes, W. Wang, I. Kravchenko, J. Valentine, *Optica* **2018**,*5*, 787.
[10] J. Karst, M. Floess, M. Ubl, C. Dingler, C. Malacrida, T. Steinle, S. Ludwigs, M. Hentschel, H. Giessen, *Science* **2021**,*374*, 612.
[11] K. Thyagarajan, R. Sokhoyan, L. Zornberg, H. A. Atwater, *Adv. Mater.* **2017**,*29*, 1701044.
[12] I.-C. Benea-Chelmus, M. L. Meretska, D. L. Elder, M. Tamagnone, L. R. Dalton, F. Capasso, *Nat. Commun.* **2021**,*12*, 5928.
[13] K. Zangeneh Kamali, L. Xu, N. Gagrani, H. H. Tan, C. Jagadish, A. Miroshnichenko, D. Neshev, M. Rahmani, *Light: Sci. Appl.* **2023**,*12*, 40.
[14] A. She, S. Zhang, S. Shian, D. R. Clarke, F. Capasso, *Sci. Adv.* **2018**,*4*, eaap9957.
[15] E. Arbabi, A. Arbabi, S. M. Kamali, Y. Horie, M. Faraji-Dana, A. Faraon, *Nat. Commun.* **2018**,*9*, 812.
[16] S. C. Malek, A. C. Overvig, S. Shrestha, N. Yu, *Nanophotonics* **2021**,*10*, 655.
[17] a) A. Forouzmand, M. M. Salary, G. K. Shirmanesh, R. Sokhoyan, H. A. Atwater, H. Mosallaei, *Nanophotonics* **2019**,*8*, 415; b) J. Park, S. J. Kim, *Appl. Opt.* **2018**,*57*, 6027.
[18] A. Forouzmand, H. Mosallaei, *Laser Photonics Rev.* **2020**,*14*, 1900353.
[19] H. Chung, O. D. Miller, *ACS Photonics* **2020**,*7*, 2236.
[20] Z. Yang, M. Liu, A. Komar, L. Xu, D. N. Neshev, *Adv. Opt. Mater.* **2022**,*10*, 2101893.
[21] S. Zhuo, Y. Li, A. Zhao, Y.-R. Li, S. Yao, M. Zhang, T. Feng, Z. Li, *Laser Photonics Rev.* **2023**,*17*, 2200403.
[22] A. Archetti, R.-J. Lin, N. Restori, F. Kiani, T. V. Tsoulos, G. Tagliabue, *Nanophotonics* **2022**,*11*, 3969.
[23] S. Joseph, S. Pandey, S. Sarkar, J. Joseph, *Nanophotonics* **2021**,*10*, 4175.
[24] a) A. Overvig, A. Alù, *Laser Photonics Rev.* **2022**,*16*, 2100633; b) Y. Zhou, S. Guo, A. C. Overvig, A. Alù, *Nano Lett.* **2023**,*23*, 6768; c) K. Shastri, F. Monticone, *Nat. Photonics* **2023**,*17*, 36.
[25] A. Kodigala, T. Lepetit, Q. Gu, B. Bahari, Y. Fainman, B. Kanté, *Nature* **2017**,*541*, 196.
[26] a) K. Koshelev, S. Kruk, E. Melik-Gaykazyan, J.-H. Choi, A. Bogdanov, H.-G. Park, Y. Kivshar, *Science* **2021**,*367*, 288; b) E. Melik-Gaykazyan, K. Koshelev, J.-H. Choi, S. S. Kruk, A. Bogdanov, H.-G. Park, Y. Kivshar, *Nano Lett.* **2020**,*21*, 1765.
[27] M. V. Rybin, K. L. Koshelev, Z. F. Sadrieva, K. B. Samusev, A. A. Bogdanov, M. F. Limonov, Y. S. Kivshar, *Phys. Rev. Lett.* **2017**,*119*, 243901.
[28] A. Tittl, A. Leitis, M. Liu, F. Yesilkoy, D.-Y. Choi, D. N. Neshev, Y. S. Kivshar, H. Altug, *Science* **2018**,*360*, 1105.
[29] G. Zograf, K. Koshelev, A. Zalogina, V. Korolev, R. Hollinger, D.-Y. Choi, M. Zuerch, C. Spielmann, B. Luther-Davies, D. Kartashov, S. V. Makarov, S. S. Kruk, Y. Kivshar, *ACS Photonics* **2022**,*9*, 567.
[30] V. Mylnikov, S. T. Ha, Z. Pan, V. Valuckas, R. Paniagua-Domínguez, H. V. Demir, A. I. Kuznetsov, *ACS Nano* **2020**,*14*, 7338.
[31] G. Yang, S. U. Dev, M. S. Allen, J. W. Allen, H. Harutyunyan, *Nano Lett.* **2001**,*22*, 2022.
[32] L. Huang, L. Xu, M. Rahmani, D. Neshev, A. Miroshnichenko, *Advanced Photonics* **2021**,*3*, 016004.
[33] E. Klopfer, S. Dagli, D. Barton, M. Lawrence, J. A. Dionne, *Nano Lett.* **2022**,*22*, 1703.
[34] M. J. A. d. Dood, A. Polman, T. Zijlstra, E. van der Drift, *J. Appl. Phys.* **2002**,*92*, 649.
[35] S. T. Thurman, G. M. Morris, *Appl. Opt.* **2003**,*42*, 3225.
[36] C. U. Hail, M. Foley, R. Sokhoyan, L. Michaeli, H. A. Atwater, *Nat. Commun.* **2023**,*14*, 8476.
[37] P. Thureja, G. K. Shirmanesh, K. T. Fountaine, R. Sokhoyan, M. Grajower, H. A. Atwater, *ACS Nano* **2020**,*14*, 15042.
[38] P. Berto, L. Philippet, J. Osmond, C. F. Liu, A. Afridi, M. Montagut Marques, B. Molero Agudo, G. Tessier, R. Quidant, *Nat. Photonics* **2019**,*13*, 649.
[39] G. Cocorullo, F. G. Della Corte, L. Moretti, I. Rendina, A. Rubino, *J. Non-Cryst. Solids* **2002**,*299*, 310.
[40] Y.-W. Huang, H. W. H. Lee, R. Sokhoyan, R. A. Pala, K. Thyagarajan, S. Han, D. P. Tsai, H. A. Atwater, *Nano Lett.* **2016**,*16*, 5319.
[41] R. Sokhoyan, P. Thureja, J. Sisler, M. Grajower, K. Shayegan, E. Feigenbaum, S. Elhadj, H. A. Atwater, *Nanophotonics* **2023**,*12*, 239.
[42] I.-C. Benea-Chelmus, S. Mason, M. L. Meretska, D. L. Elder, D. Kazakov, A. Shams-Ansari, L. R. Dalton, F. Capasso, *Nat. Commun.* **2022**,*13*, 3170.
[43] M. Nedeljkovic, R. Soref, G. Z. Mashanovich, *IEEE Photonics Journal* **2011**,*3*, 1171.

© 2024 Wiley-VCH GmbH

18638899, 2024, 6, Downloaded from https://onlinelibrary.wiley.com/doi/10.1002/lpor.202300980 by California Institute Of Technology, Wiley Online Library on [15/10/2026]. See the Terms and Conditions (https://onlinelibrary.wiley.com/terms-and-conditions) on Wiley Online Library for rules of use; OA articles are governed by the applicable Creative Commons License